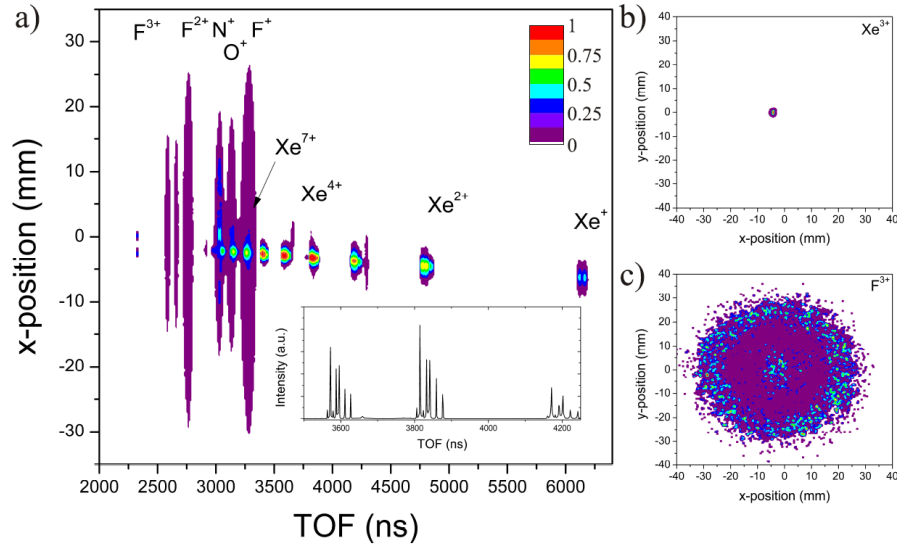
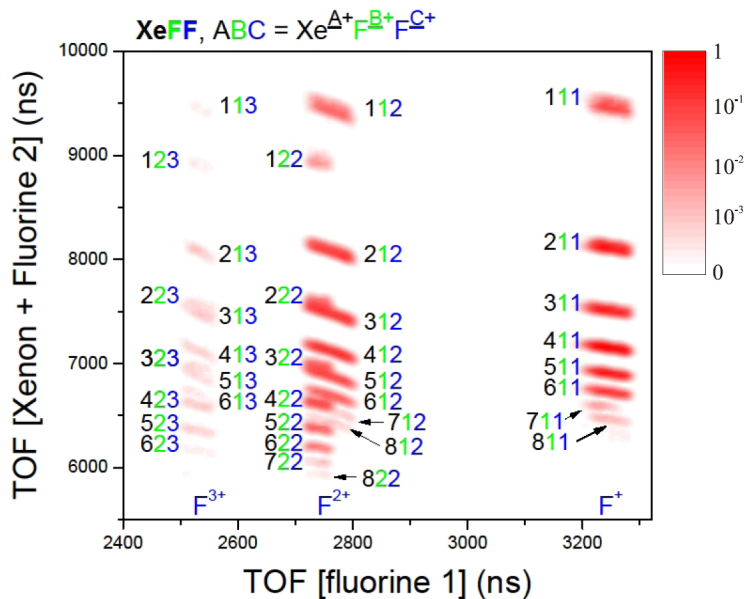


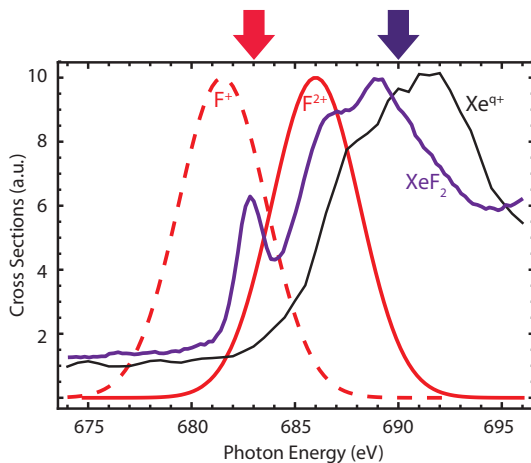
Supplementary Figure 1: Explanation of the multiple threshold method used to find the hits of the electronic traces. Panel a) shows the fitted trace using a single threshold (green dashed line); the second peak is not found. In panel b) the traces are reconstructed using five thresholds which are equally spaced. At the 3rd threshold two extra crossings, thus an extra peak, are found and the fitting code is run using this threshold instead of the first threshold. Now both peaks are found. The centers of the peaks are fitted with a Gaussian function. The experimental trace is in black, the fitted trace is in red. The blue lines indicated the tested threshold and the green line indicates the threshold that is used to find the most number of hits.



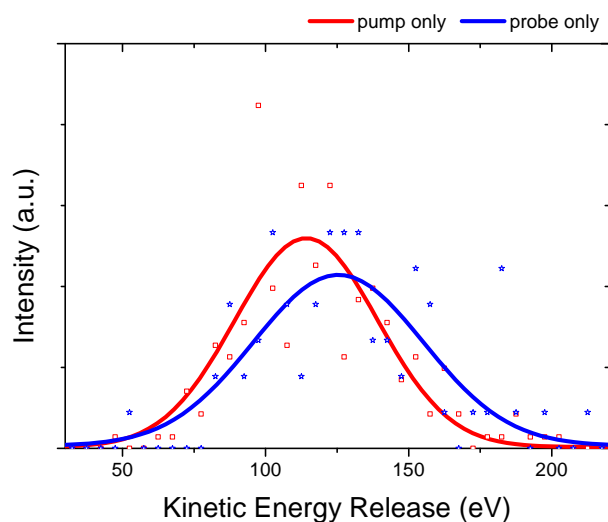
Supplementary Figure 2: Direct outcomes of our momentum imaging experiment. Panel a) displays for all ions the position on the detector along the molecular beam propagation direction as a function of time of flight (TOF). The fluorine, oxygen and nitrogen ions have a larger momentum than the xenon ions (small dots). Except for the background ions (nitrogen and oxygen), the central position (the average value of x) of the ion species decreases as the time-of-flight increases, due to the molecular beam velocity. The background ions are centered around $x=0$. The insert shows the TOF for Xe^{3+} to Xe^{5+} , and the isotopic structure is resolved. Panels b) and c) show the detector images of Xe^{3+} and F^{3+} , respectively. The molecular beam propagation direction is plotted on the x -axis and the laser propagation direction on the y -axis. The F^{3+} ions spread across the detector area due to its large momentum, while the Xe^{3+} ions show little momentum spread. The color label has been normalized to the maximum of counts: a) 16204, b) 4748, and c) 4.



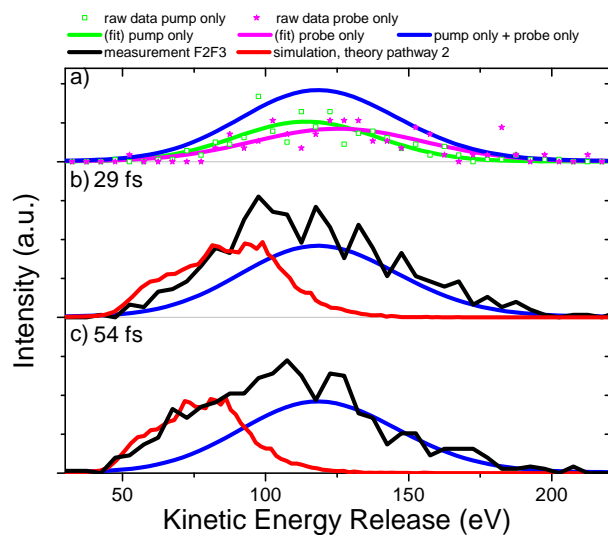
Supplementary Figure 3: Measured photoion-photoion coincidence spectra of XeF_2 obtained after application of the momentum filters. The sum of the TOF of the xenon ion plus a fluorine ion is displayed on the y-axis and the TOF of the second fluorine ion is displayed on the x-axis. The different curvatures indicate different $\text{F}^{q_1+}-\text{Xe}^{q_2+}-\text{F}^{q_3+}$ charge channels. The number of counts have been normalized with respect to the maximum of detected counts to be max 1352.



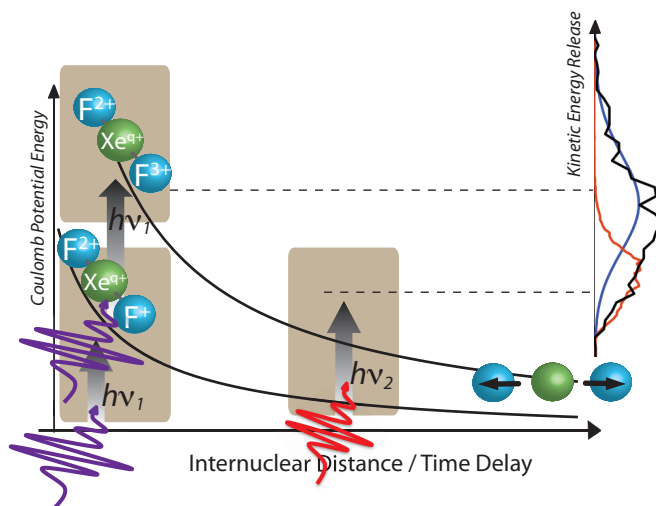
Supplementary Figure 4: Photoabsorption cross sections for the pump (purple arrow) and probe (red arrow) pulses. The cross sections are arbitrarily scaled. The neutral xenon difluoride cross section (purple curve) is taken from Ref. [8]. The $\text{Xe } 3d \rightarrow ef$ shape resonance of the molecule is pumped at 690 eV. The xenon ions Xe^{q+} cross section (black line) is taken from Ref. [15] and averaged over q^+ using the ion branching ratios of Ref. [8]. The $\text{F } 1s \rightarrow 2p$ resonances calculated with Cowan's code [13] are plotted in red. All cross sections shown are broadened by the ~ 5 -eV energy widths of the x-ray pulses. The 683-eV probe pulse excites the F^+ and F^{2+} ions formed during dissociation of the molecular ion.



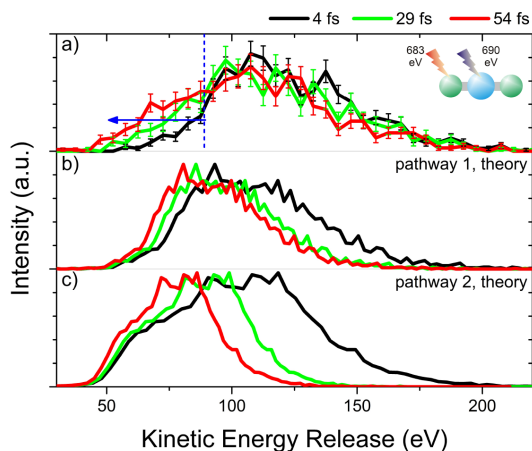
Supplementary Figure 5: KER distribution for the breakup channel (F^{2+} - Xe^{q+} - F^{3+}) when only the pump (red line) or the probe (blue line) are present.



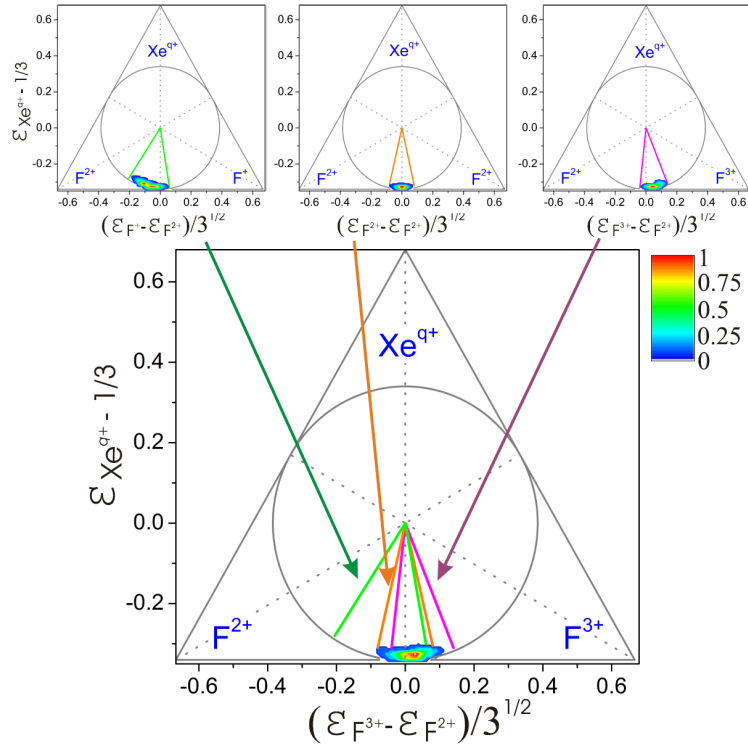
Supplementary Figure 6: KER distribution for the F^{2+} - Xe^{q+} - F^{3+} breakup channel: a) when we have only the probe (purple line) or the pump (green line) pulse. Both distributions were fitted with a Gaussian distribution and added together to show the static KER distribution (blue line). b) and c) The measured KER distribution (black line) for the pump-probe run, with 29-fs and 54-fs time delays, perfectly overlaps with the measured distributions (blue line) originating from the absorption of two photons in the same pulse, either pump or probe, and the distribution of the pump-probe events (red line, calculated with the theoretical approach explained in Supplementary Note 5).



Supplementary Figure 7: Schematic diagram for the production of the $F^{2+}-Xe^{q+}-F^{3+}$ breakup channel via pathway (2). One-photon excitation by the pump pulse excites the molecule at the Xe site at the equilibrium geometry of the neutral molecule and transfers population into the $F^{2+}-Xe^{q+}-F^+$ dissociation channel. At the 54-fs time delay, the probe excites the F^+ site and transfers population to the $F^{2+}-Xe^{q+}-F^{3+}$ potential curve. This results in the observed time-dependent KER (red line). The individual pump and probe pulses are also sufficiently intense to produce $F^{2+}-Xe^{q+}-F^{3+}$ events via sequential two-photon excitation, giving rise to a static KER distribution (blue line). The experimental results (black line) have contributions from both static and pump-probe events.



Supplementary Figure 8: X-ray pump/x-ray probe kinetic energy release distribution of the $F^{2+}-Xe^{q+}-F^{3+}$ breakup channel, averaging over all Xe charge states (average $q = +3.9$). The time delays are 4 fs (black line), 29 fs (green line), and 54 fs (red line). (a) Experimental measurements, (b) classical model following pathway (1), (c) classical model following pathway (2). The vertical dash line indicates the low energy range of KER with 20% of the distribution of the 29 fs pump probe, in which the time-dependent effects are more prominent. The events at energies left of the dashed line, shown in panel (a), are used in Supplementary Table 4.



Supplementary Figure 9: Dalitz plots of the ion momentum distributions using 690-eV pump and 683-eV probe pulses. Top three panels are the pump only distributions for $F^{2+}-Xe^{q+}-F^+$ (left), $F^{2+}-Xe^{q+}-F^{2+}$ (center), and $F^{2+}-Xe^{q+}-F^{3+}$ (right). In those cases, the momentum distribution is located towards the higher F charge states. Bottom panel: also $F^{2+}-Xe^{q+}-F^{3+}$ channel, but for the pump-probe scheme at 54 fs. This plot includes hetero-site pump-probe events coming from the pump-induced $F^{2+}-Xe^{q+}-F^+$ and $F^{2+}-Xe^{q+}-F^{2+}$ channels and results in a shift of the momentum distribution towards F^{2+} ion. Only events with KERs less than the vertical dashed line (~ 90 eV) in Supplementary Fig. 8 are plotted. The color label has been normalized to the maximum of counts, to be $\max F^{2+}F^{3+}$ (54 fs) = 6, $\max F^+F^{2+}$ (pump) = 161, $\max F^{2+}F^{2+}$ (pump) = 143, $\max F^{2+}F^{3+}$ (pump) = 9.

Supplementary Table 1: Total counts detected for uncorrelated data (no coincidence) “total Xe,F ions”, total F^{3+} ions, total coincidences events $F^{q_1+}-Xe^{q_1+}-F^{q_2+}$, and coincidences events for the breakup channel $F^{2+}-Xe^{q_1+}-F^{3+}$.

	x-ray shots	total Xe,F ions	total F^{3+}	$F^{q_1+}-Xe^{q_1+}-F^{q_2+}$	$F^{2+}-Xe^{q_1+}-F^{3+}$
4 fs	627246	3081027	32205	74244	822
29 fs	619264	2226583	27938	51198	634
54 fs	642134	2545344	26824	64180	761
Pump	448041	1398833	7042	38554	268
Probe	100807	401278	3469	9963	80

Supplementary Table 2: Number of events per shot for uncorrelated data (no coincidence) “total Xe,F ions”, total F^{3+} ions, total coincidences events $F^{q_1+}-Xe^{q_1+}-F^{q_2+}$, and coincidences events for the breakup channel $F^{2+}-Xe^{q_1+}-F^{3+}$.

	total Xe,F ions	total F^{3+}	$F^{q_1+}-Xe^{q_1+}-F^{q_2+}$	$F^{2+}-Xe^{q_1+}-F^{3+}$
4 fs	4.91	0.051	0.118	0.0013
29 fs	3.59	0.045	0.082	0.0010
54 fs	3.96	0.042	0.099	0.0012
Pump	3.12	0.016	0.086	0.0006
Probe	3.98	0.034	0.098	0.0008

Supplementary Table 3: Critical distances beyond which charge transfer cannot occur, calculated with the over-the-barrier model.

Xe^{q_1+}	$F^{q_1+}-Xe^{q_1+}-F^+ \rightarrow F^{q_1+}-Xe^{(q-1)+}-F^{2+}$	$F^{q_1+}-Xe^{q_1+}-F^{2+} \rightarrow F^{q_1+}-Xe^{(q-1)+}-F^{3+}$
	Internuclear distance (Å)	Internuclear distance (Å)
2	2.4	1.8
3	2.8	2.0
4	3.1	2.3
5	3.4	2.4
6	3.6	2.6
7	3.9	2.8
8	4.1	2.9
9	4.3	3.1

Supplementary Table 4: Areas of kinetic energy release (KER) distributions for $F^{2+}-Xe^{q_1+}-F^{3+}$ breakup channels and the ratio of areas at 54 fs and 4 fs. The measured KER distributions are plotted in Supplementary Fig. 8(a), and the % areas listed here are the areas at energies below the vertical dashed line that marks 20% of the KER distributions of the 29 fs data. The ratios of the areas at 4 fs and 54 fs show the changes in the KER distributions at short and long delays.

x rays (eV)	% area (4 fs)	% area (29 fs)	% area (54 fs)	ratio (54 fs/4 fs)
690, 683	10.8 ± 1.2	20.8 ± 2.0	29.1 ± 2.3	2.694 ± 0.013

Supplementary Note 1: X-ray pulse generation

A pump-probe experiment was performed on XeF₂ using the split undulator method described by Lutman *et al.* [1] to generate two x-ray pulses with two colors at delays of 4, 29, and 54 fs. The x-ray pulse durations were approximately 10 fs FWHM and the combined pulse energies were $\sim 33 \mu\text{J}$ before the transport optics. The pump pulse x-ray energy was centered at 690 eV and the probe pulse x-ray energy was centered at 683 eV. The pulses were generated by self-amplified spontaneous emission (SASE) and the bandwidths were ~ 5 eV FWHM.

The procedure began by generating a single 150 pC pulse with a duration of ~ 100 fs. The emittance spoiler foil [2] was used to reduce the pulse energy and duration to the levels needed for two-pulse generation. There is a trade-off between pulse energy and duration. To obtain the 10 fs pulses needed for our pump-probe experiments, the total pulse energy was reduced to $\sim 33 \mu\text{J}$.

The two-color, two-pulse generation method is described in detail in Ref. [1]. Briefly, a single electron bunch is used to generate both x-ray pulses. The bunch passes through the first 10 undulator sections to generate the pump pulse. A magnetic chicane allows a controlled delay between 0 and 50 fs, and an extra 4 fs comes from the intrinsic delay of the second color during the exponential growth through the downstream undulators. By shifting the undulator strength parameter, the x-ray energy could be shifted by up to ~ 12 eV in the energy range near 700 eV.

The x-ray pulses were first directed to the soft x-ray materials research (SXR) beamline in order to measure the x-ray energies with a grating spectrometer [3]. The SXR instrument contains a gas absorption cell. We used the Xe $3d_{5/2} \rightarrow 6p$ resonance at 674 eV for energy calibration. The two-color x-ray pulses used for the XeF₂ measurements were then observed with the SXR spectrometer and used to shift the colors and balance the pulse energies.

The two pulses were then directed to the Atomic, Molecular and Optical Science (AMO) station for the pump-probe experiments [4]. The combined x-ray pulses were microfocused onto the target molecular beam by Kirkpatrick-Baez mirrors. Spatial overlap of the two pulses was adjusted by viewing their images with CCD cameras on screens inserted in the beam path.

With the two pulse energies calibrated, overlapped, and focused in the chamber, the pump-probe delay could be adjusted and either the pump or probe pulse removed. In that way, a set of measurements were made using pump-only, probe-only, and pump-probe delays of 4, 29, and 54 fs.

Supplementary Note 2: Data acquisition and analysis

The ions, produced by the interaction of both x-ray pulses with the target molecules, were projected onto a time- and position-sensitive detector, a hexanode delay-line detector (RoentDek HEX80), by a homogeneous DC electric field (483 V/cm), which allowed for an optimal collection efficiency (angular acceptance) for the energetic (fluorine) fragments but limited the kinetic energy resolution of the xenon ions. For each shot the 7 electronic traces (MCP, u1, u2, v1, v2, w1, w2) of the hexanode detector were saved by Acqiris pulse digitization boards with 500 ps time resolution. The traces were analyzed using the CASS-CFEL-ASG software suite [5]. However, we implemented our own ‘‘Center-of-Mass’’ method using multiple thresholds instead of a single threshold which allow recovering ‘‘double peak structures’’, see Supplementary Fig. 1, due to fluorine ions arriving to the detector at similar time. The multiple-threshold method recovers around 5% more hits (mainly due to an extra peak in the double peak structure).

The hits of the 7 traces were converted into x,y,t coordinates using the reconstruction code of Roentdek [6]. The three-dimensional (3D) momentum vectors of each detected ionic fragment were reconstructed from the x,y,t coordinates. Subsequently the XeF₂ molecular ion breakup channels were reconstructed by applying momentum conservation. A filter was set for all directions separately as well as for the total momentum: $dp_x = 55$ a.u., $dp_y = 75$ a.u., $dp_z = 36$ a.u., $dp_{xyz} = 70$ a.u.). The momenta are used to calculate the kinetic energy of each ion, and the kinetic energies of three ions in a breakup channel allow determining the total kinetic energy release (KER), sum of each kinetic energy. The error in kinetic energy release is 1.2 eV (standard deviation). The three ion momentum distributions are plotted in Dalitz and Newtons plots.

Supplementary Fig. 2 depicts the position on the detector along the molecular beam propagation direction as a function of time of flight (TOF). The TOFs of all ions are plotted along with the detector xy images of the F³⁺ and Xe³⁺ ions. Note that in the TOF, the central position (the average value of x) of ion species decreases as the time-of-flight increases, due to the molecular beam velocity. After the breakup, all the fragments have an additional velocity in the x-direction due to the molecular beam velocity, and the fragments with more TOF (time to reach the detector) present larger shifts in the x-direction. The events coming from nitrogen and oxygen molecules do not display this effect, because those molecules are from the background gas and not the molecular beam. One way to display the three-ion coincidences is to plot the TOF of one F ion vs. the sum of the TOFs of the other F ion and

the Xe ion. These PiPiCo spectra are shown in Supplementary Fig. 3.

In Supplementary Table 1, we show the x-ray shots during the three different runs at 4-fs, 29-fs, and 54-fs time delays, but also when we have only the pump and only the probe, with the corresponding uncorrelated data (no coincidence) “total Xe,F ions”, total F^{3+} ions, total coincidences events for $F^{q_1+}-Xe^{q_2+}-F^{q_3+}$, and coincidences for the breakup channel $F^{2+}-Xe^{q_1+}-F^{3+}$. The latter is the channel discussed in detail in the main manuscript.

From this table, we can divide the detected ions and coincidences per the number of shots to get an idea of the number of events per pulse/shot, see Supplementary Table 2.

Supplementary Note 3: Cross sections and transition rates

Using the two-color/two-pulse method of Ref. [1] to generate the x-ray pulses, the photon energy separation between the two colors was limited to ~ 12 eV in the energy range near 700 eV. That was a factor in choosing XeF_2 for a hetero-site-specific experiment, because the Xe $3d_{5/2}$, Xe $3d_{3/2}$, and F $1s$ ionization energies (679.31 eV, 692.09 eV, and 691.23 eV, respectively [7]) are within that tuning range. Also, we had previously studied charge redistribution and ion fragmentation of XeF_2 induced by Xe K -shell photoionization [21]. Another consideration is that measurements on XeF_2 can be compared with measurements and calculations on atomic Xe. In preparation for the present pump-probe experiment, we measured photoionization cross sections and partial ion yields of Xe and XeF_2 from Xe $3d_{5/2}$, Xe $3d_{3/2}$, and F $1s$ subshells in the 660-740 eV range [8]. Results of those measurements were used to help guide the LCLS experiment.

The goal was to trigger Xe $3d$ photoionization and core-hole decay with the pump pulse and then probe the emerging F ions during the dissociation of the molecular ion. The estimated photoabsorption cross sections for the pump and probe pulses are shown in Supplementary Fig. 4. The cross sections are arbitrarily scaled to each other, but they show the resonant features which led us to choose the 690-eV pump and 683-eV probe energies. The cross section for ground-state XeF_2 is from the measurements of Ref. [8]. The 690-eV pump energy is near the maximum of the Xe $3d_{5/2} \rightarrow \epsilon f$ shape resonance, and a strong F $1s \rightarrow$ LUMO (lowest unoccupied molecular orbital) resonance is observed at the 683-eV probe energy [8]. The LUMO is a delocalized anti-bonding MO with large components of Xe $5p$ and F $2p$ orbitals [8, 12].

A quantitative description of how the XeF_2 orbitals are correlated with the states of the fragment ions following x-ray absorption is required to develop an accurate model of the transient states. The absorption cross sections of the transient states of the x-ray-pumped molecule are not known and are quite difficult to calculate, because they involve high charge states and ultrafast nuclear motion. Although these states have some molecular character, we estimated the cross sections of the x-ray-pumped molecule by a combination of atomic cross sections of the Xe and F ions. Experimentally, we probed the emerging F^+ and F^{2+} ions near their $1s \rightarrow 2p$ resonances. These are calculated to be at ~ 681.5 and ~ 686 eV [13, 14], respectively, and both have large oscillator strengths. The calculated resonances are plotted in Supplementary Fig. 4 after broadening with the ~ 5 -eV width of the probe pulse. The absolute cross sections for $3d$ photoionization of the low charge states of Xe have been measured by a merged photon-ion technique [15]. Using the measured Xe^{q+} branching ratios of Ref. [8] and the cross sections of Ref. [15], a weighted-average Xe^{q+} cross section was derived and is plotted in Supplementary Fig. 4. The Xe^{q+} cross section maximum shifts up in energy and the probability of exciting the Xe site with the probe pulse at 683 eV is reduced.

The 690-eV pump pulse triggers Xe $3d$ photoionization of XeF_2 and a multi-step Auger cascade that induces breakup of the molecular ion to a range of Xe charge states and F ions [8]. The 683-eV probe pulse can then excite the $1s \rightarrow 2p$ resonance of either F^+ or F^{2+} that emerge during the breakup process. There is no experimental data for the photoionization yields of the $1s \rightarrow 2p$ resonance in fluorine atom, but there is for atomic nitrogen and oxygen. The single-, double-, and triple-charge-state yields following $1s \rightarrow 2p$ photoexcitation of atomic nitrogen [16] and atomic oxygen [17] have been measured. Single ionization is dominant, but the double-ionization yields are $\sim 20\%$. We propose that a combination of Auger decay and shakeoff will similarly result in single and double ionization of the F^+ and F^{2+} ions excited at their $1s \rightarrow 2p$ resonances.

Supplementary Note 4: Understanding the measured KER

In this note we present the KER distributions for the runs in which we have only the pump pulse or only the probe pulse, see Supplementary Fig. 5. Note that this breakup channel is induced by the absorption of two photons, hence, both the pump and probe are intense enough for inducing two-photon sequential processes. Because of the limited beamtime, the pump-only and probe-only data were recorded for shorter measurement periods than the three

pump-probe runs. Despite the large statistical errors, the KER ranges can be determined and are roughly the same. The difference in the observed pump-only and probe-only distributions could simply reflect the counting statistics.

In the experimental data, we have contributions from different two-photon processes: i) when two photons are absorbed from the pump pulse, ii) when two photons are absorbed from the probe pulse, and iii) when one photon is absorbed from the pump pulse and one photon is absorbed from the probe pulse (pump-probe signal). It should be noted that two-photon events from either the pump or the probe are always present in the measured data for all pump-probe runs, whereas the simulations do not include such background (static, no time-dependent) events. In Supplementary Fig. 6, we have combined the measured KER for $F^{2+}-Xe^{q+}-F^{3+}$, and the theoretical calculations for the pump-probe events. First, we fit the measured events of the pump and the probe with a Gaussian profile and we add their corresponding broadening. Then, the corresponding fit is plotted together with the theoretical calculations for the pump-probe events, and both distributions perfectly overlap with the measured $F^{2+}-Xe^{q+}-F^{3+}$ events of the pump-probe runs.

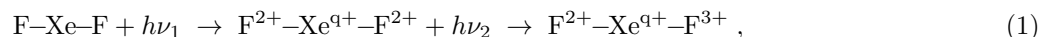
Supplementary Fig. 7 illustrates the mechanism of pathway (2). The pump excites the molecule at the Xe site at the equilibrium distance of the neutral molecule and populates the $F^{2+}-Xe^{q+}-F^+$ channel. At a certain time delay, the probe excites the transient states of the molecule at the F site and transfers population from the $F^{2+}-Xe^{q+}-F^+$ channel to the $F^{2+}-Xe^{q+}-F^{3+}$ channel. Because the $F^{2+}-Xe^{q+}-F^+$ channel has already begun to dissociate, the probe excitation occurs at larger internuclear distances, where the slope of the $F^{2+}-Xe^{q+}-F^{3+}$ potential is much smaller than at short range, resulting in a KER feature that shifts to lower energies with increasing time delay.

Supplementary Note 5: Classical breakup model

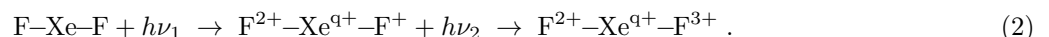
The response of a molecule after the absorption of a x-ray photon is highly nonperturbative, presenting various electron and nuclear processes that are involved in the inner-shell hole relaxation. In heavy elements such as the xenon atom, the creation of 3d inner-shell holes mainly induces a multi-step cascade of Auger processes, i.e. a sequential emission of Auger electrons. Those processes produce a range of charge states, from Xe^+ up to Xe^{8+} [19, 20]. In XeF_2 molecule, the removal of a Xe 3d electron will also trigger the multi-step cascade of Auger processes. The first steps of the Auger processes are localized in the Xe site. However, the late stages of the Auger cascade, in contrast with Xe atom, involve delocalized valence electrons that spread charge to neighboring atomic sites. In previous studies of XeF_2 molecules [21], the kinetic energies of the F fragment ions suggested that ion dissociation begins while the Auger cascade is still in progress and charge is developing on the system. Other experiments that measure ion fragments in coincidence also suggest that charge production, charge redistribution, and ion dissociation proceed concurrently in molecular systems [22, 23]. The present experiment is designed to observe x-ray induced electronic and nuclear dynamics in progress.

A quantum-mechanical model of the inner-shell hole decay dynamics is very challenging for theory and computational methods. In general, it involves several charge states, with a wide range of excited electronic states, and with strong nuclear dynamics that cannot be neglected. Therefore, in order to model the hetero-site pump-probe signal observed in the KER, we need to resort to a less complete model and make some approximations to reduce the complexity of the dynamics.

By using a model based on classical interactions (Newton equations for charged particles), we are able to qualitatively describe the time dependence observed in the $F^{2+}-Xe^{q+}-F^{3+}$ breakup channel, as shown in Supplementary Fig. 8. In the classical model, the probe pulse can either excite the F^+ or the F^{2+} ion. Therefore, the probe can induce population transfer either from the $F^{2+}-Xe^{q+}-F^+$ or the $F^{2+}-Xe^{q+}-F^{2+}$ channels into the $F^{2+}-Xe^{q+}-F^{3+}$ channel. Note that the ions may not be in the ground ionic states during the breakup process. Resonant excitation from the probe pulse will result in the charge states increasing by 1 or 2 by a combination of Auger and shake-off processes. In measurements on atomic oxygen and nitrogen at the $1s \rightarrow 2p$ resonances, singly, doubly, and triply charged ions are produced [16, 17]. The doubly charged yields are $\sim 20\%$ of the singly charged yields. Hence, we can identify two pathways contributing to the $F^{2+}-Xe^{q+}-F^{3+}$ breakup channel. The first pathway follows



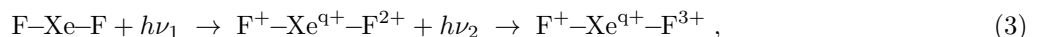
while the second pathway follows



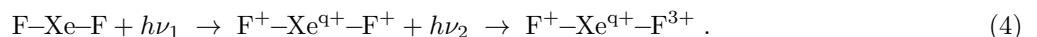
By using classical-motion equations, each KER of $F^{2+}-Xe^{q+}-F^+$ and $F^{2+}-Xe^{q+}-F^{2+}$ channels can be mapped onto an initial distribution (the total kinetic energy is converted to Coulomb potential energy). Here we assume that the initial internuclear distances between Xe and the two F are equal. For the $F^{2+}-Xe^{q+}-F^+$ and $F^{2+}-Xe^{q+}-F^{2+}$ channels

we obtain an internuclear distance distribution between 1.96 - 5.47 Å and 2.01 - 4.13 Å, respectively, compared with the equilibrium distance of the neutral molecule at 1.97 Å. The model indicates that the $F^{2+}-Xe^{q+}-F^{2+}$ channel is generally formed at later stages of the Auger cascade, when the molecule has already started to dissociate, and the ions of the breakup channel are formed when the internuclear distance is larger than the equilibrium distance. Similarly, the $F^{2+}-Xe^{q+}-F^+$ channel is generally formed when the molecule is dissociating, but it can also be formed near the equilibrium distance. The KER distribution induced by the probe pulse is calculated by evolving the charged particles for every internuclear distance in the initial distribution during the three time delays. The differential equation given by three point-like charges separated by a certain internuclear distance and repelling each other by the Coulomb force is solved by a Runge-Kutta method. Note that no molecular potential curve is considered, i.e. the potential is taken to be purely Coulombic. After a specific time delay, we assume that the probe instantly increases the charge of a F particle, plus one or two, and we obtain a $F^{2+}-Xe^{q+}-F^{3+}$ KER distribution, see Supplementary Fig. 8. For simplicity, our simulations do not account for the ~ 10 fs pulse durations or the ~ 4 fs lifetime of F 1s holes. The classical simulations qualitatively reproduce the time dependence in the measured KERs. As mentioned above, the doubly charged yields are expected to be $\sim 20\%$ of the singly charged yields. On the other hand, our measurements of the charge-state yields of the pump pulse show a relative ratio of around 4 times more $F^{2+}-Xe^{q+}-F^+$ than $F^{2+}-Xe^{q+}-F^{2+}$. In addition, from atomic calculations, we expect similar absorption cross sections at 683 eV for the excitation of F^+ and F^{2+} ions. Hence, contributions from the two pathways are similar.

We also observed a hetero-site pump-probe signal in the $F^+-Xe^{q+}-F^{3+}$ channel. We can also use the classical breakup model for this particular channel. Two pathways can be identified, following



and



The classical model is also used to calculate the population transfer $F^+-Xe^{q+}-F^+ \rightarrow F^+-Xe^{q+}-F^{2+}$, but in this case the time-dependent pump-probe signals lie within the $F^+-Xe^{q+}-F^{2+}$ KER distribution created only by the pump pulse. Thus, the model also gives an explanation why in the experimental data no time dependence is observed in the $F^+-Xe^{q+}-F^{2+}$ KER distribution.

Supplementary Note 6: Over-the-barrier classical model

In this section we discuss the time scales for charge redistribution initiated by the pump excitation. To obtain a quantum-mechanical description of the charge redistribution during the inner-shell hole relaxation is quite challenging, and we will need to calculate Auger decay rates for a large manifold of electronic transient states at different internuclear distances. In addition, we will also need to consider the nuclear motion of the molecule in addition to changes in the valence electron density. There is currently no code available to describe such quantum-mechanical dynamics. Instead, we can borrow a classical ‘‘over-the-barrier’’ model from ion scattering experiments that has been proven to work very well to describe charge redistribution during inner-shell excitation [22]. That model allows the estimation of the critical internuclear distances of XeF_2 ion breakup channels at which charge redistribution cannot occur energetically, see Supplementary Table 3.

For reference, the equilibrium distance of the neutral XeF_2 molecule is 1.97 Å. In a breakup channel with Xe^{4+} , an electron located in a F^+ ion can be transferred to the Xe ion at distances less than 3.1 Å, while an electron located in a F^{2+} ion can only be transferred to the Xe ion at distances less than 2.3 Å. However, if we consider the classical breakup channel of $F^+-Xe^{4+}-F^+$, the internuclear distances at time delays of 4 fs, 29 fs, and 54 fs will be 2.04 Å, 4.39 Å, and 8.01 Å, respectively. Therefore, this model provides an estimate of when charge redistribution is not possible. For all the breakup channels, charge transfer is likely at 4 fs, but far less so for the time delays 29 fs and 54 fs. In order to convince ourselves that this will be the general rule, we can consider a ‘‘slow-dissociative’’ breakup channel, $F^+-Xe^{2+}-F^+$, for which the internuclear distances at 4 fs, 29 fs, and 54 fs will be 2.01 Å, 3.41 Å, and 5.81 Å, respectively.

Obviously, this model is simplified, as we should also consider Auger decay rates (the first Auger transitions will be very fast, only a few femtoseconds) and the pulse length of the pulses (around 10 fs). However, the calculated values with the ‘‘over-the-barrier’’ model are sufficient to make the general statement that charge redistribution is possible at 4-fs time delays, small at 29-fs time delays, and nonexistent at 54-fs time delays. These estimates are important for analyzing the time-dependent features observed in the KER distributions of the $F^{2+}-Xe^{q+}-F^{3+}$ channel, as it eliminates the possibility that the observed pump-probe signal comes from absorption of the probe at the Xe site followed by a charge redistribution to the fluorine sites.

Supplementary Note 7: Additional statistics for time-dependent KER

In this note we present additional analysis of our results for the $F^{2+}-Xe^{q+}-F^{3+}$ breakup channel. In Supplementary Fig. 8 we show the KERs for the three pump-probe time delays. The position of the vertical dashed line indicates the lowest 20% of the KER of the 29-fs pump-probe data. This is the region showing the most prominent time-dependent effects. The areas below the dashed line are smaller for the 4-fs pump-probe data and larger for the 54-fs pump-probe data. The ratios of those areas are listed in Supplementary Table 4 and show a clear time dependence.

Supplementary Note 8: Understanding ion-momentum distributions

For the analysis of the linear momentum distribution, we use Dalitz plots [23, 24], which are a functional way to visualize momentum distributions of a three-body break-up. In the main manuscript we already show the effects of the hetero-site pump-probe signal. Here we show additional Dalitz plots to support the discussed results. The top panels of Supplementary Fig. 9 show the Dalitz plots for the $F^{2+}-Xe^{q+}-F^+$, $F^{2+}-Xe^{q+}-F^{2+}$, and the $F^{2+}-Xe^{q+}-F^{3+}$ channels when only the pump pulse is present. In the $F^{2+}-Xe^{q+}-F^+$ and the $F^{2+}-Xe^{q+}-F^{3+}$ plots the momentum distributions are shifted towards the F^{2+} and F^{3+} ion, respectively. This is expected from a simultaneous classical break-up of a linear triatomic molecule with asymmetric charges (and equal mass). In the bottom panel, we observe the Dalitz plot also for the $F^{2+}-Xe^{q+}-F^{3+}$ channel, but for the hetero-site pump-probe data with a time delay of 54 fs. In general, the momentum distribution is also shifted toward the F^{3+} ion, similar to the case when only the pump is present. However, in the pump-probe distribution at 54 fs, we observe a small contribution emerging toward the F^{2+} ion. This contribution comes from the hetero-site pump-probe events, in which the interaction of the probe pulse transfers population from the $F^{2+}-Xe^{q+}-F^+$ and $F^{2+}-Xe^{q+}-F^{2+}$ channels to the $F^{2+}-Xe^{q+}-F^{3+}$ channel, in agreement with the top two left figures.

Supplementary References

- [1] A. A. Lutman, R. Coffee, Y. Ding, Z. Huang, J. Krzywinski, T. Maxwell, M. Messerschmidt, and H.-D. Nuhn, “Experimental demonstration of femtosecond two-color x-ray free-electron lasers,” *Phys. Rev. Lett.* **110**, 134801 (2013).
- [2] P. Emma, K. Bane, M. Cornacchia, Z. Huang, H. Schlarb, G. Stupakov, and D. Walz, “Femtosecond and subfemtosecond x-ray pulses from a self-amplified spontaneous-emission-based free-electron laser,” *Phys. Rev. Lett.* **92**, 074801 (2004).
- [3] P. Heimann, O. Krupin, W. F. Schlotter, J. Turner, J. Krzywinski, F. Sorgenfrei, M. Messerschmidt, D. Bernstein, J. Chalupský, V. Hájková, S. Hau-Riege, M. Holmes, L. Juha, N. Kelez, J. Lüning, D. Nordlund, M. F. Perea, A. Scherz, R. Soufli, W. Wurth, and M. Rowen, “Linac Coherent Light Source soft x-ray materials science instrument optical design and monochromator commissioning,” *Rev. Sci. Instrum.* **82**, 093104 (2011).
- [4] K. R. Ferguson, M. Bucher, J.D. Bozek, S. Carron, J.-C. Castagna, R. Coffee, G. I. Curiel, M. Holmes, J. Krzywinski, M. Messerschmidt, M. Minitti, A. Mitra, S. Moeller, P. Noonan, T. Osipov, S. Schorb, M. Swiggers, A. Wallace. J. Yin, and C. Bostedt, “The atomic, molecular and optical science instrument at the Linac Coherent Light Source,” *J. Synchrotron Rad.* **22**, 492-497 (2015).
- [5] L. Foucar, A. Barty, N. Coppola, R. Hartmann, P. Holl, U. Hoppe, S. Kassemeyer, N. Kimmel, J. Küpper, M. Scholz, S. Teichert, T. A. White, L. Strüder, and J. Ullrich, “CASS-CFEL-ASG software suite,” *Comp. Phys. Comm.* **183**, 2207-2213 (2012).
- [6] O. Jagutzki, A. Cerezo, A. Czasch, R. Dörner, M. Hattass, M. Huang, V. Mergel, U. Spillmann, K. Ullmann-Pfleger, T. Weber, H. Schmidt-Böcking, G. D. W. Smith, “Multiple hit readout of a microchannel plate detector with a three-layer delay-line anode”, *IEEE Trans. Nucl. Sci.* **49**, 2477-2483 (2002).
- [7] T. X. Carroll, R. W. Shaw, Jr., T. D. Thomas, C. Kindle, and N. Bartlett, “Electron distribution in the xenon fluorides and xenon oxide tetrafluoride by ESCA and evidence for “orbital independence” in the xenon-fluorine bonding,” *J. Am. Chem. Soc.* **96**, 1989-1996 (1974).
- [8] S. H. Southworth, R. Wehlitz, A. Picón, C. S. Lehmann, L. Cheng, and J. F. Stanton, “Inner-shell photoionization and core-hole decay of Xe and XeF₂,” *J. Chem. Phys.* **142**, 224302 (2015).
- [9] N. Saito and I. H. Suzuki, “Yields of multicharged Xe ions in the M-shell transition region,” *J. Phys. B At. Mol. Opt. Phys.* **25**, 1785-1793 (1992).
- [10] U. Arp, K. Iemura, G. Kutluk, T. Nagata, S. Yagi, and A. Yagishita, “3d photoionization of Xe, Cs and Ba and the collapse of the 4f wavefunction,” *J. Phys. B At. Mol. Opt. Phys.* **32**, 1295-1304 (1999).
- [11] A. Kivimäki, U. Hergenhahn, B. Kempgens, R. Hentges, M. N. Piancastelli, K. Maier, A. Rüdél, J. J. Tulkki, and A. M. Bradshaw, “Near-threshold study of Xe 3d photoionization,” *Phys. Rev. A* **63**, 012716 (2000).
- [12] H. Basch, J. W. Moskowitz, C. Hollister, and D. Hankin, “Self-Consistent-Field Study of the Series XeF_n, n = 2, 4, 6,” *J. Chem. Phys.* **55**, 1922-1933 (1971).
- [13] R. D. Cowan, *The theory of atomic structure and spectra*, Los Alamos Series in Basic and Applied Sciences (University of California Press, Berkeley, 1981) ISBN 9-780-520-03821-9.
- [14] Los Alamos National Laboratory, Atomic Physics Codes, <http://aphysics2.lanl.gov/tempweb/lanl/>.
- [15] S. Schippers, S. Ricz, R. Buhr, A. Borovik Jr., J. Hellhund, K. Holste, K. Huber, H.-J. Schäfer, D. Schury, S. Klumpp, K. Mertens, M. Martins, R. Flesch, G. Ulrich, E. Rühl, T. Jahnke, J. Lower, D. Metz, L. P. H. Schmidt, M. Schöffler, J. B. Williams, L. Glaser, F. Scholz, J. Seltmann, J. Viehhaus, A. Dorn, A. Wolf, J. Ullrich, and A. Müller, “Absolute cross sections for photoionization of Xe^{q+} ions (1 ≤ q ≤ 5) at the 3d ionization threshold,” *J. Phys. B At. Mol. Opt. Phys.* **47**, 115602 (2014).
- [16] M. M. Sant’Anna, A. S. Schlachter, G. Öhrwall, W. C. Stolte, D. W. Lindle, and B. M. McLaughlin, “K-shell x-ray spectroscopy of atomic nitrogen,” *Phys. Rev. Lett.* **107**, 033001 (2011).
- [17] B. M. McLaughlin, C. P. Ballance, K. P. Bowen, D. J. Gardenghi, and W. C. Stolte, “High precision K-shell photoabsorption cross sections for atomic oxygen: experiment and theory,” *Astrophys. J. Lett.* **771:L8** (2013) and Erratum **779:L31** (2013).
- [18] C. D. Caldwell, S. J. Schaphorst, M. O. Krause, and J. Jiménez-Mier, “Photoexcited K Auger spectra of atomic and molecular oxygen,” *J. Electron Spectrosc.* **67**, 243-259 (1994).
- [19] V. Jonauskas, L. Partanen, S. Kučas, R. Karazija, M. Huttula, S. Aksela, and H. Aksela, “Auger cascade satellites following 3d ionization in xenon,” *J. Phys. B At. Mol. Opt. Phys.* **36**, 4403-4416 (2003).
- [20] L. Partanen, R. Sankari, S. Osmekhim, Z. F. Hu, E. Kukk, and H. Aksela, “Multiple ionization of Xe - comparison of de-excitation pathways following 3d_{5/2} ionization and 3d_{5/2} → 6p resonance excitation,” *J. Phys. B At. Mol. Opt. Phys.* **38**, 1881-1893 (2005).
- [21] R. W. Dunford, S. H. Southworth, D. Ray, E. P. Kanter, B. Krässig, L. Young, D. A. Arms, E. M. Dufresne, D. A. Walko, O. Vendrell, S.-K. Son, and R. Santra, “Evidence for interatomic Coulombic decay in Xe K-shell-vacancy decay of XeF₂,” *Phys. Rev. A* **86**, 033401 (2012).
- [22] B. Erk, R. Boll, S. Trippel, D. Anielski, L. Foucar, B. Rudek, S. W. Epp, R. Coffee, S. Carron, S. Schorb, K. R. Ferguson, M. Swiggers, J. D. Bozek, M. Simon, T. Marchenko, J. Küpper, I. Schlichting, J. Ullrich, C. Bostedt, D. Rolles, and A. Rudenko, “Imaging charge transfer in iodomethane upon x-ray photoabsorption,” *Science* **345**, 288-291 (2014).
- [23] R. Guillemin, P. Decleva, M. Stener, C. Bomme, T. Marin, L. Journal, T. Marchenko, R. K. Kushawaha, K. Jänkälä, N. Trcera, K. P. Bowen, D. W. Lindle, M. N. Piancastelli, and M. Simon, “Selecting core-hole localization or delocalization in CS₂ by photofragmentation dynamics,” *Nat. Commun.* **6**, 6166 (2015).
- [24] R. H. Dalitz, “Decay of τ mesons of known charge,” *Phys. Rev.* **94**, 1046-1051 (1954).